Price, SH, Bezanson, R, Labbe, I, Furtak, LJ, de Graaff, A, Greene, JE, Kokorev, V, Setton, DJ, Suess, KA, Brammer, G, Cutler, SE, Leja, J, Pan, R, Wang , B , Weaver, JR, Whitaker, KE, Atek, H, Burgasser, AJ, Chemerynska, I, Dayal, P, Feldmann, R, Förster Schreiber, NM, Fudamoto, Y, Fujimoto, S, Glazebrook, K, Goulding, AD, Khullar, G, Kriek, M, Marchesini, D, Maseda, MV, Miller, TB, Muzzin, A, Nanayakkara, T, Nelson, E, Oesch, PA, Shipley, H, Smit, R, Taylor, EN, Dokkum, PV, Williams, CC and Zitrin, A

The UNCOVER Survey: First Release of Ultradeep JWST/NIRSpec PRISM Spectra for ∼700 Galaxies from z ∼ 0.3–13 in A2744

Price, Sedona H., Bezanson, Rachel, Labbe, Ivo, Furtak, Lukas J., de Graaff, Anna, Greene, Jenny E., Kokorev, Vasily, Setton, David J., Suess, Katherine A., Brammer, Gabriel, Cutler, Sam E., Leja, Joel, Pan, Richard, Wang, Bingjie, Weaver, John R., Whitaker, Katherine E., Atek, Hakim, Burgasser, Adam J., Chemerynska, Iryna, Dayal, Pratika, Feldmann, Robert, Förster Schreiber, Natascha M., Fudamoto, Yoshinobu, Fujimoto, Seiji, Glazebrook, Karl, Goulding, Andy D., Khullar, Gourav, Kriek, Mariska, Marchesini, Danilo, Maseda, Michael V., Miller, Tim B., Muzzin, Adam, Nanayakkara, Themiya, Nelson, Erica, Oesch, Pascal A., Shipley, Heath, Smit, Renske, Taylor, Edward N., Dokkum, Pieter van, Williams, Christina C. and Zitrin, Adi

The UNCOVER Survey: First Release of Ultradeep JWST/NIRSpec PRISM Spectra for ~700 Galaxies from z ~ 0.3–13 in A2744

The Astrophysical Journal, 982:51 (16pp), 2025 March 20 https://doi.org/10.3847/1538-4357/adaec1

The UNCOVER Survey: First Release of Ultradeep JWST/NIRSpec PRISM Spectra for ∼700 Galaxies from $z \sim 0.3$–13 in A2744

Sedona H. Price[1], Rachel Bezanson[1], Ivo Labbe[2], Lukas J. Furtak[3], Anna de Graaff[4], Jenny E. Greene[5], Vasily Kokorev[6], David J. Setton[5,30], Katherine A. Suess[7,31], Gabriel Brammer[8], Sam E. Cutler[9], Joel Leja[10,11,12], Richard Pan[13], Bingjie Wang (王冰洁)[10,11,12], John R. Weaver[9], Katherine E. Whitaker[8,9], Hakim Atek[14], Adam J. Burgasser[15], Iryna Chemerynska[14], Pratika Dayal[16], Robert Feldmann[17], Natascha M. Förster Schreiber[18], Yoshinobu Fudamoto[19], Seiji Fujimoto[6,31], Karl Glazebrook[2], Andy D. Goulding[5], Gourav Khullar[1], Mariska Kriek[20], Danilo Marchesini[13], Michael V. Maseda[21], Tim B. Miller[22], Adam Muzzin[23], Themiya Nanayakkara[2], Erica Nelson[24], Pascal A. Oesch[8,25], Heath Shipley[26], Renske Smit[27], Edward N. Taylor[2], Pieter van Dokkum[28], Christina C. Williams[29], and Adi Zitrin[3]

[1] Department of Physics and Astronomy and PITT PACC, University of Pittsburgh, Pittsburgh, PA 15260, USA
[2] Centre for Astrophysics and Supercomputing, Swinburne University of Technology, Melbourne, VIC 3122, Australia
[3] Physics Department, Ben-Gurion University of the Negev, P.O. Box 653, Be'er-Sheva 84105, Israel
[4] Max-Planck-Institut für Astronomie, Königstuhl 17, D-69117 Heidelberg, Germany
[5] Department of Astrophysical Sciences, Princeton University, 4 Ivy Lane, Princeton, NJ 08544, USA
[6] Department of Astronomy, The University of Texas at Austin, Austin, TX 78712, USA
[7] Kavli Institute for Particle Astrophysics and Cosmology and Department of Physics, Stanford University, Stanford, CA 94305, USA
[8] Cosmic Dawn Center (DAWN), Niels Bohr Institute, University of Copenhagen, Jagtvej 128, København N, Copenhagen DK-2200, Denmark
[9] Department of Astronomy, University of Massachusetts, Amherst, MA 01003, USA
[10] Department of Astronomy & Astrophysics, The Pennsylvania State University, University Park, PA 16802, USA
[11] Institute for Computational & Data Sciences, The Pennsylvania State University, University Park, PA 16802, USA
[12] Institute for Gravitation and the Cosmos, The Pennsylvania State University, University Park, PA 16802, USA
[13] Department of Physics and Astronomy, Tufts University, 574 Boston Avenue, Medford, MA 02155, USA
[14] Institut d'Astrophysique de Paris, CNRS, Sorbonne Université, 98bis Boulevard Arago, 75014 Paris, France
[15] Department of Astronomy & Astrophysics, University of California San Diego, La Jolla, CA, USA
[16] Kapteyn Astronomical Institute, University of Groningen, 9700 AV Groningen, The Netherlands
[17] Department of Astrophysics, University of Zurich, Zurich CH-8057, Switzerland
[18] Max-Planck-Institut für extraterrestrische Physik, Giessenbachstrasse 1, 85748 Garching, Germany
[19] Center for Frontier Science, Chiba University, 1-33 Yayoi-cho, Inage-ku, Chiba 263-8522, Japan
[20] Leiden Observatory, Leiden University, P.O. Box 9513,NL-2300 AA Leiden, The Netherlands
[21] Department of Astronomy, University of Wisconsin-Madison, 475 N. Charter Street, Madison, WI 53706, USA
[22] Center for Interdisciplinary Exploration and Research in Astrophysics (CIERA), Northwestern University, 1800 Sherman Avenue, Evanston, IL 60201, USA
[23] Department of Physics and Astronomy, York University, 4700 Keele Street, Toronto, Ontario, ON MJ3 1P3, Canada
[24] Department for Astrophysical and Planetary Science, University of Colorado, Boulder, CO 80309, USA
[25] Department of Astronomy, University of Geneva, Chemin Pegasi 51, 1290 Versoix, Switzerland
[26] Department of Physics, Texas State University, San Marcos, TX 78666, USA
[27] Astrophysics Research Institute, Liverpool John Moores University, 146 Brownlow Hill, Liverpool L3 5RF, UK
[28] Astronomy Department, Yale University, 219 Prospect Street, New Haven, CT 06511, USA
[29] NSF's National Optical-Infrared Astronomy Research Laboratory, 950 North Cherry Avenue, Tucson, AZ 85719, USA
Received 2024 August 7; revised 2024 December 5; accepted 2024 December 21; published 2025 March 18

Abstract

We present the design and observations of low-resolution JWST/NIRSpec PRISM spectroscopy from the Ultradeep NIRSpec and NIRCam ObserVations before the Epoch of Reionization (UNCOVER) Cycle 1 JWST Treasury program. Targets are selected using JWST/NIRCam photometry from UNCOVER and other programs, and cover a wide range of categories and redshifts to ensure the legacy value of the survey. These categories include the first galaxies at $z \gtrsim 10$, faint galaxies during the Epoch of Reionization ($z \sim 6-8$), high-redshift active galactic nuclei ($z \gtrsim 6$), Population III star candidates, distant quiescent and dusty galaxies ($1 \lesssim z \lesssim 6$), and filler galaxies sampling redshift–color–magnitude space from $z \sim 0.1-13$. Seven NIRSpec microshutter array masks across the extended A2744 cluster were observed, along with NIRCam parallel imaging in nine filters (F090W, F115W, F150W, F200W, F277W, F356W, F410M, F444W, and F480M) over a total area of $\sim$26 arcmin^2, overlapping existing Hubble Space Telescope coverage from programs including the Hubble Frontier Fields and BUFFALO. We successfully observed 553 objects down to $m_{\rm F444W} \sim 30$ AB, and by leveraging mask overlaps, we reach total on-target exposure times ranging from 2.4 to 16.7 hr. We demonstrate the success rate and distribution of the confirmed redshifts, and also highlight the rich information revealed by these ultradeep spectra for a subset of our targets. An updated lens model of A2744 is also presented, including 14 additional

[30] Brinson Prize Fellow.
[31] NHFP Hubble Fellow.

spectroscopic redshifts and finding a total cluster mass of $M_{\rm SL} = (2.1 \pm 0.3) \times 10^{15}\, M_{\odot}$. We publicly release reduced 1D and 2D spectra for all objects observed in summer 2023 along with a spectroscopic redshift catalog and the updated lens model of the cluster (https://jwst-uncover.github.io/DR4.html).

Unified Astronomy Thesaurus concepts: Galaxy evolution (594); Galaxy formation (595); High-redshift galaxies (734)

Materials only available in the online version of record: machine-readable table

1. Introduction

Deep JWST imaging from early programs has already begun to revolutionize our understanding of the faint, distant Universe. The observatory has met or exceeded nearly every preflight expectation (M. J. Rieke et al. 2023), and early data have enabled us to find and begin characterizing many galaxy populations that were previously inaccessible: from the first generation of galaxies at Cosmic Dawn (e.g., R. P. Naidu et al. 2022; H. Atek et al. 2023; S. L. Finkelstein et al. 2023; B. E. Robertson et al. 2023; C. M. Casey et al. 2024; B. Robertson et al. 2024), to the faint galaxies driving the reionization of the Universe at $z \sim 6$–9 (e.g., P. G. Pérez-González et al. 2023), to early quiescent galaxies at $z \sim 3$–5 (e.g., A. C. Carnall et al. 2023a; F. Valentino et al. 2023). JWST imaging also provides new insights into galaxies' detailed structures (at $z \lesssim 6$; e.g., L. Ferreira et al. 2022, 2023; J. S. Kartaltepe et al. 2023; M. Martorano et al. 2023; E. J. Nelson et al. 2023; A. van der Wel et al. 2024, among many others), including reaching low stellar masses approaching those of the dwarf galaxy population ($M_* \sim 10^6\, M_{\odot}$; e.g., K. A. Suess et al. 2023) and revealing the structures of heavily dust-obscured galaxies, which were previously observable only in the submillimeter (e.g., V. Kokorev et al. 2023; S. H. Price et al. 2023; Y. Wu et al. 2023). Ultradeep JWST imaging has additionally enabled detections of possible globular clusters as early as $z \sim 1.4$ (e.g., L. Mowla et al. 2022; A. Claeyssens et al. 2023; D. A. Forbes & A. J. Romanowsky 2023), as well as more detailed studies of globular clusters within galaxies out to at least $z \sim 0.3$ (e.g., W. E. Harris & M. Reina-Campos 2023, 2024). Early JWST imaging has also yielded surprises, including larger than anticipated numbers of very luminous early galaxies (e.g., R. P. Naidu et al. 2022; H. Atek et al. 2023; D. Austin et al. 2023; L. D. Bradley et al. 2023; S. L. Finkelstein et al. 2023; N. J. Adams et al. 2024; C. M. Casey et al. 2024; I. Chemerynska et al. 2024b; B. Robertson et al. 2024) and an unexpected, relatively numerous population of obscured active galactic nucleus (AGN) candidates at high redshift (e.g., L. J. Furtak et al. 2023a; I. Labbe et al. 2023; G. Barro et al. 2024; V. Kokorev et al. 2024; C. C. Williams et al. 2024).

Taking the next step in exploring these newly uncovered parameter spaces requires leveraging JWST's spectroscopic capabilities to both confirm the galaxies' redshifts and to probe their internal physical properties in detail. Even with the high sensitivity of JWST/NIRSpec (T. Böker et al. 2023), pushing to the most distant and faint regimes is best accomplished with very deep observations in cluster fields, where the strong gravitational lensing boost reaches intrinsically fainter populations by 1–2 mag relative to blank fields. Complementing the aforementioned imaging results, spectra from early JWST programs have already revealed new discoveries and unprecedented measurements. Results from this early spectroscopy include confirming the redshifts and properties of galaxies at $z \gtrsim 9$ (e.g., P. Arrabal Haro et al. 2023a, 2023b; E. Curtis-Lake et al. 2023; G. Roberts-Borsani et al. 2023), and confirming and characterizing high-redshift obscured AGN (e.g., Y. Harikane et al. 2023; R. Maiolino et al. 2023; J. Matthee et al. 2024) as well as quiescent galaxies at $z \gtrsim 3$ (e.g., A. C. Carnall et al. 2023b, 2024; A. de Graaff et al. 2024b; K. Glazebrook et al. 2024).

The Ultradeep NIRSpec and NIRCam ObserVations before the Epoch of Reionization (UNCOVER) Cycle 1 Treasury survey (R. Bezanson et al. 2024) was designed to collect these deep spectra early in the JWST mission. UNCOVER was designed to obtain ultradeep, multiband NIRCam imaging, photometrically detect and characterize galaxies down to $\mathrm{mag}_{\rm F444W} \sim 30$ AB (J. R. Weaver et al. 2024), and then select targets from these newly observable populations for follow-up ultradeep NIRSpec/PRISM multiobject spectroscopy (P. Ferruit et al. 2022). The low-resolution PRISM mode provides both high sensitivity and wide spectral coverage (i.e., T. Böker et al. 2023), enabling us to constrain continuum breaks down to ∼29 AB and measure rest-frame ultraviolet (UV) to near-infrared (NIR) emission and absorption features raging from galaxies within the cluster itself at $z \sim 0.3$ out to the earliest epochs at $z \gtrsim 10$. Early UNCOVER spectroscopic results already address many of these aims, including finding objects among the first generation of galaxies (e.g., B. Wang et al. 2023a), characterizing distant obscured AGN (e.g., J. E. Greene et al. 2024), and uncovering early quiescent galaxy formation (e.g., D. J. Setton et al. 2024).

In this paper we present an overview of the UNCOVER NIRSpec/PRISM spectroscopic observations of 668 targets in the A2744 strong lensing (SL) cluster field, as well as our coordinated parallel NIRCam imaging which overlaps with existing Hubble Space Telescope (HST) observations from the Hubble Frontier Fields (HFF; J. M. Lotz et al. 2017) and BUFFALO (C. L. Steinhardt et al. 2020) programs. We detail the target selection, mask design, and the observations (Section 2), and the spectroscopic reduction and redshift measurements (Section 3). We also present the redshift success rate and distribution of measured redshifts, and discuss example cases of spectra addressing the scientific objectives of the UNCOVER survey (Section 4). This paper accompanies the public release of early reduced NIRSpec/PRISM spectra, spectroscopic redshifts, and the NIRCam parallel imaging. All magnitudes given are in the AB system (J. B. Oke 1974).

2. Spectroscopic Observations

2.1. Target Selection

Targets are primarily selected from photometric catalogs constructed from all publicly available HST and JWST imaging over A2744 as of 2023 June. The JWST/NIRCam observations are: UNCOVER (PIs: Labbe and Bezanson, JWST-GO-2561; R. Bezanson et al. 2024), the Early Release Science program GLASS (PI: Treu, JWST-ERS-1324; T. Treu et al. 2022), and a Director's Discretionary program (PI: Chen, JWST-DD-2756), providing a total of eight filters: F090W, F115W, F150W, F200W, F277W, F356W, F410M, and F444W. The archival HST data consist of HST-GO-11689 (PI: Dupke), HST-GO-13386 (PI: Rodney), HST-DD-13495 (PI: Lotz; J. M. Lotz et al. 2017), and HST-GO-15117 (PI: Steinhardt; C. L. Steinhardt et al. 2020), providing coverage in seven filters: F435W, F606W, F814W, F105W, F125W, F140W, and F160W. The majority of the targets are selected from the UNCOVER NIRCam-selected catalog (as presented in J. R. Weaver et al. 2024), using internal version v2.2.0. This version, containing ~50,000 objects down to a combined long-wavelength (LW; F277W + F356W + F444W) depth of ~30.5 AB in the deepest regions, included improved treatment of point-spread function (PSF) homogenization and estimates of total magnitudes compared to the initial public Data Release 1 (2023 January).[32] While selecting targets, UNCOVER stellar population modeling including Prospector-β and EAZY were considered (as in J. R. Weaver et al. 2024; B. Wang et al. 2024). However, the default UNCOVER catalogs excluded a small number of interesting sources, e.g., highly lensed, multiply imaged and/or shredded objects. In these cases, targets were added by hand (with target IDs > 60000). Furthermore, a subset of the targets were selected based on information from other wavelengths, including Atacama Large Millimeter/submillimeter Array (ALMA) submillimeter/millimeter (DUALZ, PI: Fujimoto, S. Fujimoto et al. 2023; ALCS, PI: Kohno, S. Fujimoto et al. 2023b; ALMA Frontier Fields, PI: Bauer; A. M. Muñoz Arancibia et al. 2023) and Chandra X-ray (e.g., Á. Bogdán et al. 2024) observations.

For target selection, the updated version of the L. J. Furtak et al. (2023b) analytic lens model of A2744 was used (`v1.1`).[33] This version includes one additional multiple image system in the northern substructure (system 82), and more importantly, an additional spectroscopic redshift in the northwestern substructure from new Very Large Telescope (VLT)/MUSE observations of the cluster (system 68 at $z = 2.584$, P. Bergamini et al. 2023a; see also Appendix B.2). The `v1.1` lens model achieved a lens plane average image reproduction rms of $\Delta_{\rm rms} = 0\farcs51$.

As the UNCOVER science goals cover a wide range of topics, including potentially risky unknowns, the final spectroscopic targeting is complex. The prioritization scheme for assigning targets to masks is as follows. Categories corresponding to the originally proposed science cases (see R. Bezanson et al. 2024) are roughly prioritized corresponding to rarity and scientific value: (1) any $z > 12$ candidates, (2) $z > 9$ galaxies prioritized by brightness, (3) Population III candidate sources, (4) faint highly magnified $6 < z < 7$ galaxies,[34] (5) $z > 4$ quiescent galaxies, (6) $z > 6$ AGN, (7) $z > 4$ dusty galaxies, and other galaxies with ALMA detections (e.g., S. Fujimoto et al. 2023), (8) low-mass quiescent galaxies at $1 < z < 6$, (9) any unusual or unexpected sources, (10) extreme emission line galaxies, and finally (11) mass-selected "filler" galaxies sampled in bins of redshift, mass, and F150W − LW color (using the LW noise-equalized F277W + F356W + F444W image, and EAZY-derived mass and redshifts). For these filler targets, the numerical priority class n was set to be proportional to the $\log^2$ inverse of the cumulative surface density in each property. As the mask design software eMPT (N. Bonaventura et al. 2023) maps priority class n to weight according to a $1/2^n$ weighting scheme, this approximately equates to an importance sampling scheme that is flat in color, magnitude, and redshift (i.e., sparsely sampling regions of parameter space with many objects, and densely sampling where objects are less common).

2.2. Mask Designs and Observations

The NIRSpec/PRISM observations are split into seven MSA mask configurations, with per-mask exposure times of 2.6–4.4 hr (see Table 1). As shown in Figure 1, these masks cover the UNCOVER NIRCam primary footprint, with overlaps allowing for repeated observations of faint, high-priority targets. The masks were designed iteratively using eMPT (N. Bonaventura et al. 2023), designing each mask in sequence according to target priority, then modifying the priorities to ensure targets requiring deeper integrations are placed on additional masks until the required exposure time is met. This procedure was repeated using hand-specified mask positions until an optimal design (in terms of both number of highest priority targets and total number of targets) was reached. In total, 668 unique targets are assigned to masks, with total planned exposure times ranging from 2.6 to 17.4 hr.

The NIRSpec observations were taken on 2023 July 31–August 2, with the 2-POINT-WITH-NIRCam-SIZE2 dither pattern and a three-shutter slitlet nod pattern. The NIRSpec NRSIRS2RAPID and NRSIRS2 readout patterns were adopted for Masks 1–3 and 4–7, respectively. Coordinated parallel NIRCam imaging was also taken (as described in Appendix A). The observations were taken with a V3PA angle ~266° or NIRSpec MSA aperture PA ~ 44.°56 (see exact values in Table 1), to ensure efficient MSA coverage over the UNCOVER NIRCam footprint and to overlap the parallel NIRCam imaging with existing HST/Advanced Camera for Surveys (ACS) and WFC3 observations from the HFF (J. M. Lotz et al. 2017) and BUFFALO (C. L. Steinhardt et al. 2020) programs.

An electrical short early in Visit 1 severely impacted both detectors, with complete loss for most sources and severely reduced data quality in a minority of objects; repeat observations of a slightly modified Mask 1 (due to small differences in PA) were approved, and were observed on 2024 July 30–31. Additionally, an SSR drive exception (relating to drive space) impacted the Visit 3 observations, leading to a loss of 7% of the NIRSpec integration time in Mask 3 (one frame each for both detectors; yielding a total exposure of 2.4 hr) as well as 66% of the NIRCam parallel imaging (all of F150W, F200W, F356W, and F444W). Repeat observations of the NIRCam parallel for Visit 3 (in all six filters, given a probable observing PA change) were also approved, and observed on 2024 July 31. All repeat observations will be included in a future release. Given these setbacks, and a small percentage of failed reduction/extractions or other data quality issues, here we present robust spectra for 553 objects, with exposure times of 2.4–16.7 hr.

[32] The published versions of R. Bezanson et al. (2024) and J. R. Weaver et al. (2024) include further improvements, corresponding to public Data Release 2 (DR2; equivalent to internal release v3.0.1). Photometric redshifts and stellar masses were derived using EAZY (G. B. Brammer et al. 2008; see J. R. Weaver et al. 2024) and Prospector-β (B. Wang et al. 2023b; see B. Wang et al. 2024).

[33] The `v1.1` deflection maps are publicly available on the UNCOVER website: https://jwst-uncover.github.io/DR2.html#LensingMaps.

[34] We emphasize that many of the faint, highly magnified sources remain very small and are compact sources for the NIRSpec microshutter array (MSA; and not "arcs").

Table 1
NIRSpec MSA Masks

Mask	Exposure	R.A.$_{\rm center}$	Decl.$_{\rm center}$	PA$_{\rm MSA}$	$N_{\rm target}$
	(hr)			(deg)	
(1)	(2)	(3)		(4)	(5)
1	2.6[a]	3.5839128	−30.3998611	44.5711	129
2	2.6	3.6084098	−30.3911336	44.5548	116
3	2.4[b]	3.5732805	−30.3686750	44.5568	136
4	4.4	3.5586419	−30.3564067	44.5719	146
5	4.4	3.5808445	−30.3723050	44.5608	144
6	4.4	3.5803516	−30.3721636	44.5611	147
7	2.9	3.5808445	−30.3723050	44.5608	146

Notes. The sample includes 668 unique targets, with some targets on multiple masks. Column (1): mask number. Column (2): mask exposure time (units of hr). Column (3): mask center R.A. and decl. (J2000). Column (4): MSA position angle (PA, in degrees). Column (5): number of targets on mask.
[a] The effective total exposure time for Mask 1 is much shorter than the on-sky time, given an electrical short (see Section 2.2). Repeat observations of Mask 1 were taken 2024 July 30–31.
[b] The final frame in Visit 3 (Mask 3) for both detectors was lost due to the solid state recorder (SSR) drive exception.

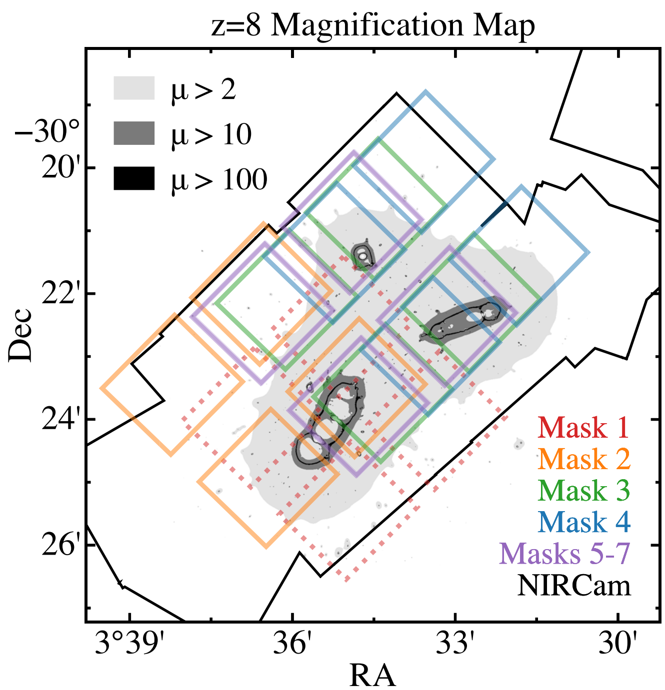

Figure 1. UNCOVER NIRSpec MSA mask footprints within the A2744 cluster field. Shaded regions denote the regions of magnification $\mu > 2$, 10, and 100 (grayscale, light to dark) from the updated UNCOVER lensing maps (v2.0) for a source at redshift $z_s = 8$, and existing NIRCam coverage (from Cycle 1 imaging) is shown with the black outline. The masks, shown with colored outlines, span most of the imaging footprint over a range of low- and high-magnification regions. The electrical-short-impacted Mask 1 is marked with a dotted outline. (Note Masks 5–7 have near-complete overlap.)

3. Spectroscopic Reduction and Redshift Measurements

3.1. Spectroscopic Reduction and 1D Extraction

The PRISM spectra are reduced using `msaexp` (v0.8.5; G. Brammer 2023a), `grizli` (v1.11.9; G. Brammer 2023b), and the JWST `jwst` pipeline (v1.14.0; H. Bushouse et al. 2024) using the `jwst_1241.pmap` reference files. Level 1 products are downloaded from MAST,[35] and then `msaexp` (using `grizli`) runs the `jwst` Stage 1 pipeline, inserting the `snowblind`[36] (J. Davies 2024) improved "snowball" identification and correction procedure after the jump step. `msaexp` next applies a $1/f$ correction, and, finally, a median pedestal bias offset of the science data (SCI extension) and multiplicative scaling factor to the read noise array (RNOISE extension) are calculated from empty parts of each exposure that should not have any contribution from sky or source photons. Further steps of the `jwst` Stage 2 pipeline are then run to assign the world coordinate system, flag open microshutters, identify and extract 2D slits, apply slit-level flat-fielding, correct for vignetting of the MSA bars, and apply the photometric calibration.

For this first spectroscopic data release, local background subtraction is performed by taking differences of the 2D spectrum arrays at the different telescope nod positions.[37] This local background subtraction is performed on the original 2D slitlet cutouts before performing drizzle resampling. `msaexp` then rectifies the 2D spectra from each exposure and resamples them into a final stack with an algorithm analogous to DRIZZLE (A. S. Fruchter & R. N. Hook 2002), adopting a pixel fraction and wavelength sampling of 1.0. In contrast to the STScI `jwst` drizzle resampling algorithm, the spectra here are only rectified along the columns of the cross-dispersion axis and all wavelength bins are kept fully independent, which eliminates the correlated noise in the dispersion direction that results from a full 2D drizzle resampling.

The final 1D spectra are then extracted from the local background-subtracted 2D spectra using an optimal extraction (K. Horne 1986) scheme, modified to account for the variable spatial resolution across the full PRISM wavelength range. This modified extraction uses a 2D profile, consisting of independent 1D Gaussians in the cross-dispersion spatial direction over the full wavelength range (and not a single, uniform cross-dispersion profile as used in the standard optimal extraction scheme). The 1D spatial cross-dispersion profile at every wavelength is a pixel-integrated Gaussian with width equal to the sum in quadrature of the PSF width (at that wavelength) and an intrinsic cross-

[35] Available from 10.17909/8k5c-xr27.

[36] https://github.com/mpi-astronomy/snowblind

[37] This scheme can lead to issues for cases with objects/intracluster light (ICL) light falling within the flanking shutters, which we discussed later in this section.

dispersion object width. This intrinsic width is determined by fitting a model with parameters for both the intrinsic profile width and a spatial offset (relative to the position expected from the mask and input catalog metadata) to the curved traces of the original spectral cutouts (accounting for wavelength-dependent PSF broadening). As this fit is performed using the full 2D traces, intrinsic widths can be determined for objects with detected continua and/or emission lines (even if only emission lines, and not any continuum, is detected). For faint objects with little to no signal (for either lines or the continuum), the inferred intrinsic width will be close to the initial guess (here, 0.7 pixels). The final 2D profile (with varying spatial profile as a function of wavelength) used for optimal extraction is rebinned and rectified in the same way as the science data, and the optimally weighted extraction is performed in the rectified frame. This 2D modified optimal extraction profile is included in an extension in the reduced spectra fits files.

Path-loss corrections computed by `msaexp` are included in the final spectra. Using the predicted position of the object within the shutter and assuming the object has an axisymmetric (i.e., round) Gaussian shape with the same intrinsic width measured from the cross-dispersion profiles (as described above), `msaexp` determines the fraction of light falling within the slit for a source of this size and position relative to a perfectly centered point source. This path-loss factor is determined as a function of wavelength (accounting for the variable PSF), and is then used to correct the reduced spectra.[38]

We note that we have not attempted to apply any aperture corrections (beyond the path-loss correction described above) —that is, any corrections to account for what portion of the target is captured within the slit, particularly with respect to how the target's photometry has been measured. In some cases, it may be beneficial for users to derive a wavelength-dependent aperture correction when jointly modeling photometry and spectroscopy. For instance, if a target is very off center in the dispersion (x) direction of the slit or when only a small fraction of the entire object lies within the slit, such a correction would account for differences in photometric and spectroscopic aperture position and size. One approach to derive such a correction would be to determine a scaling between the spectrum and photometry (e.g., using a wavelength-dependent polynomial that is fit by comparing the scaled-spectrum photometric-filter-convolved fluxes to the observed fluxes), which avoids any detailed calculations (e.g., regarding the slit position or fraction of the object within the slit). However, such an approach neglects the presence of color gradients (due to spatially variable stellar populations or dust, or portions with/without an AGN component, among other possibilities). Furthermore, such a spectrum-to-photometry scaling would likely require extrapolation, given the very wide PRISM wavelength coverage. To facilitate such aperture corrections the user may choose to apply, or to enable extracting photometry in the same apertures as the slits, we include a catalog detailing the shutter positions of all targets on all masks as part of this data release. The source position within the shutter is also stored in the spectrum FITS header, as are the intrinsic cross-dispersion width and cross-dispersion extraction center.[39]

The "local" background-subtraction scheme adopted for this release assumes that the flanking shutters of the three-microshutter slitlets represent a reasonable approximation of the background within the shutter in which the target is centered. This assumption breaks down for large objects which fill multiple adjacent microshutters (resulting in partial "self-subtraction"), or in cases where nearby objects or light from bright cluster galaxies or the ICL fall within these flanking shutters, leading to contamination of the background estimate. We estimate whether each object is impacted by this issue by determining whether light from any object (either the target itself or a neighbor) or from the ICL/bright cluster galaxies falls within the neighboring shutters (defined as the regions with surface brightness brighter than the target's surface brightness in F444W at its effective radius, from Sérsic fits if available or from the source extraction half-light radii otherwise). The flag `flag_potential_local_background_issue` is included in the released redshift catalog (see Section 3.2 and Table 2) to alert users of such potential background-subtraction issues. We emphasize that background-subtraction issues do not preclude the measurement of robust redshifts, nor that the spectrum cannot be used —this flag is only advisory, indicating that users should examine the 2D spectrum and 1D extraction profile to determine if the degree and nature of background contamination will impact their analysis. Future releases will include global background-subtracted spectra (with the background determined accounting for positional variations and any low-order wavelength dependence) for all objects, and will be the default recommended spectrum for such large objects and those with other contamination of the neighboring shutters.

Finally, we note that some objects are observed on multiple masks. In the current reduction, all frames of a target are directly combined during the reduction, implicitly assuming that the slitlets of different masks cover the same spatial region of that source. We also note that for this first release, spectra from the short-impacted Mask 1 are not reduced. The spectra from the repeat observation of Mask 1, and t hose taken along with the repeat of the Visit 3 NIRCam parallel imaging, will be included in future spectroscopic releases.

3.2. Spectroscopic Redshifts and Line Fluxes

The spectroscopic redshifts for this data release are determined from the reduced, full-depth 1D spectra using `msaexp`. First, redshift fits are performed using the EAZY (G. B. Brammer et al. 2008) `corr_sfhz_13` galaxy template set with a wide allowed redshift range (z = [0.05, 14]). A second redshift fit is then performed with a library of spectral lines and cubic splines for a flexible continuum model, restricted within $\pm 0.03(1 + z)$ of the template best-fit redshift (or within the range z = [0.05, 14] if the template fit failed). Models for the emission lines are generated in `msaexp` as pixel-integrated Gaussians with widths taken from the wavelength-dependent spectral resolution curve provided by

[38] While the path-loss correction does account for wavelength-dependent light losses of extended targets based on their position, the assumptions of axisymmetry (leveraging the cross-dispersion size) and a smooth light distribution will not entirely capture each source's complex morphology. More extensive path-loss modeling based on multiwavelength morphology or scaling to same-aperture-extracted photometry are possible approaches to perform aperture correction that better accounts for these issues.

[39] Specified by "SRCXPOS" and "SRCYPOS" (in units of shutter width/height, with 0 = centered), and "PROFSIG" and "PROFCEN" (relative to the cross-dispersion center of the 2D spectrum), in units of pixels.

Table 2
Redshift Catalog from UNCOVER NIRSpec/PRISM Spectra

id_msa	ra	dec	z_spec	z_spec16	z_spec50	z_spec84	flag_zspec_qual	flag_successful_spectrum	flag_potential_local_background_issue	flag_emission_lines	flag_line_and_break	flag_break_strong_abs_features_only	flag_break_only	flag_stellar_bump_only	method_best_zfit	method_zuncert	texp_tot	masks	id_DR3	sep_DR3
(1)	(2)		(3)	(4)	(5)	(6)	(7)	(8)	(9)	(10)	(11)	(12)	(13)	(14)	(15)	(16)	(17)	(18)	(19)	(20)
mr 2008	3.59242259	−30.43282858	…	…	…	…	0	0	1	…	…	…	…	…	…	…	0.0	1	10065	0.009
2044	3.58615595	−30.43309276	…	…	…	…	0	0	1	…	…	…	…	…	…	…	0.0	1	10155	0.017
2354	3.58522511	−30.43136947	…	…	…	…	0	0	0	…	…	…	…	…	…	…	0.0	1	10730	0.009
2385	3.58064554	−30.43128230	…	…	…	…	0	0	1	…	…	…	…	…	…	…	0.0	1	10787	0.021
43197	3.59312594	−30.34885302	3.791	3.788	3.793	3.798	3	1	0	1	0	0	0	0	spl + lines	templ	4.4	4	55712	0.005
43239	3.57603883	−30.34966523	0.172	0.170	0.171	0.173	2	1	1	0	0	0	0	1	templ	templ	7.3	5, 7	56010	0.099
43311	3.56381835	−30.34873405	3.291	3.285	3.289	3.294	3	1	0	1	0	0	0	0	spl + lines	templ	7.3	5, 7	55788	0.002
43388	3.56605332	−30.34854295	3.801	3.795	3.801	3.806	3	1	0	1	0	0	0	0	spl + lines	templ	7.3	5, 7	55908	0.006

Notes. The full table is available from https://jwst-uncover.github.io/DR4.html and on Zenodo (DR4.1.1) doi:10.5281/zenodo.14559840. Column (1): MSA ID (corresponding to internal v2.2.0). Column (2): targeted R.A. and decl. (internal v2.2.0 catalog; J2000, decimal degrees). Column (3): spectroscopic redshift. Columns (4)–(6): 16/50/84th percentile from redshift fit $p(z)$ distribution. Column (7): redshift quality flag: 3 = secure, based on two or more secure spectral features (e.g., two robustly detected emission lines, one clear break and one robust emission line, two robustly detected absorption features); 2 = solid, based on one broad continuum feature or two less robust features (e.g., a break or stellar bump, or two marginally detected emission lines, or one marginally detected emission lines and a break); 1 = tentative but unreliable redshift; and 0 = no redshift. For analysis, using redshifts with quality flag = 3 or = 2 is recommended. Column (8): spectrum flag: 1 = successfully observed and reduced spectrum; and 0 = no spectrum/data quality issue. Column (9): local background-subtraction issue flag: 1 = objects with potential issues from galaxy/ICL light in the neighboring shutters; and 0 = no local background-subtraction issues. This flag does not preclude the measurement of robust redshifts, nor the use of this spectrum for science analysis—rather this is an advisory flag to alert users to inspect the 2D spectrum and evaluate if this background issue could impact their planned analysis. Column (10): feature flag, for spectra containing two or more emission lines (1 = yes, 0 = no). Column (11): feature flag, for spectra containing a break + an emission line (1 = yes, 0 = no). Column (12): feature flag, for spectra containing only a break and strong absorption features (1 = yes, 0 = no). Column (13): feature flag, for spectra containing only a break (1 = yes, 0 = no). Column (14): feature flag, for spectra containing only a stellar bump (1 = yes, 0 = no). Column (15): fit method for best-fit redshift. templ = template, spl+lines = spline+lines; see Section 3.2. Column (16): fit method for redshift uncertainties/percentiles (see column (15)). Column (17): total exposure time (hr). Column (18): list of masks on which each object was included (comma separated string). Column (19): closest match Data Release 3 (DR3) ID (K. A. Suess et al. 2024; B. Wang et al. 2024; J. R. Weaver et al. 2024). Column (20): separation of DR3 and MSA R.A./decl., in arcseconds.

(This table is available in its entirety in machine-readable form in the online article.)

STScI and used by the JWST exposure time calculator ($R \sim 50$ at 1.5 μm, $R \sim 300$ at 5 μm;[40] jwst nirspec prism disp.fits). The prism disperser does not spectrally resolve typical galaxy emission lines, though extremely broad emission (e.g., due to broad-line AGN or outflows) can be resolved.

The spectroscopic redshift for each object is determined as follows: (1) from the template fit, for objects with only continuum features based on visual inspection (i.e., only breaks or stellar bumps and no emission lines); or else (2) from the lines + splines fit, if at least one emission line is detected with signal-to-noise ratio (S/N) $\geqslant 3$ in that fit (and the target was not flagged as only having continuum features in visual inspection); or finally (3) from the template fit, if no line is detected. The redshift uncertainties for all targets are taken from the 16th and 84th percentiles of the full redshift range template fit (or from the lines + splines fit, if the template fit failed).

The redshift fits are examined by multiple (minimum of three) team members, and flagged based on the number and robustness of the detected spectral features, as described in Table 2. The redshift quality flag, `flag_zspec_qual`, denotes secure redshifts (= 3; from two or more secure spectral features, e.g., two robustly detected emission lines, one clear break and one robust emission line, two robustly detected absorption features), solid redshifts (=2; from one broad continuum feature, either a break or stellar bump, or from two less robust features, e.g., two marginally detected emission lines or one marginally detected emission line and a break), tentative but unreliable redshifts (=1), and no redshift solution (=0). The flag `flag_successful_spectrum` is also included, indicating whether the target spectrum was successfully observed and reduced (=1) or not (=0; due to data quality issues or missing spectra).

In select cases identified during the visual fit inspection (14 objects; 2.5%), the redshifts are manually refit with alternative settings (i.e., multiple robust emission lines where the initial template fits yielded inaccurate redshift estimates; or noise is misidentified as lines when the redshifts are more robustly measured from template fits to continuum breaks) or are fixed (the three brown dwarfs at $z_{\rm spec} = 0$; see Section 4.2). The redshift quality flag is updated based on these modified redshift solutions.

In addition to spectroscopic redshifts, we also determine line fluxes from the `msaexp` fits for each object. We adopt the values from the same fit as the best-fit redshift (described above). The reported line fluxes are not corrected for lensing magnification.

Accompanying this paper, we publicly release reduced spectra and spectroscopic redshifts from the UNCOVER NIRSpec/MSA observations taken in summer 2023.[41] This data release (UNCOVER Data Release 4 (DR4)) includes the 1D optimally extracted spectra and the 2D spectra with local background subtraction, for all successfully reduced spectra. The redshift catalog for this release (described in Table 2 and the downloadable machine-readable format version) includes the measured redshifts (if any), redshift and spectra quality flags (including an advisory flag indicating potential issues in the local background subtraction, as discussed in Section 3.1—here we emphasize again that this flag does not preclude the measurement of robust redshifts, but that it is intended to alert users that they should examine the spectra to determine whether the local background will impact their analysis), the total exposure time, and the assigned masks for the full set of targeted objects. Subsequent spectroscopic releases will include the observations from the repeated Visits 1 and 3 and both global and local background-subtracted spectra (optimized for extended and point sources, respectively) and an updated redshift catalog.

Reduced mosaics of the NIRCam parallel observations are also available, constructed following the same procedures as the cluster NIRCam observations (except that modeling and subtraction of bright cluster galaxy and ICL is not performed). Full details about the parallel mosaics are presented in the UNCOVER survey paper (R. Bezanson et al. 2024).

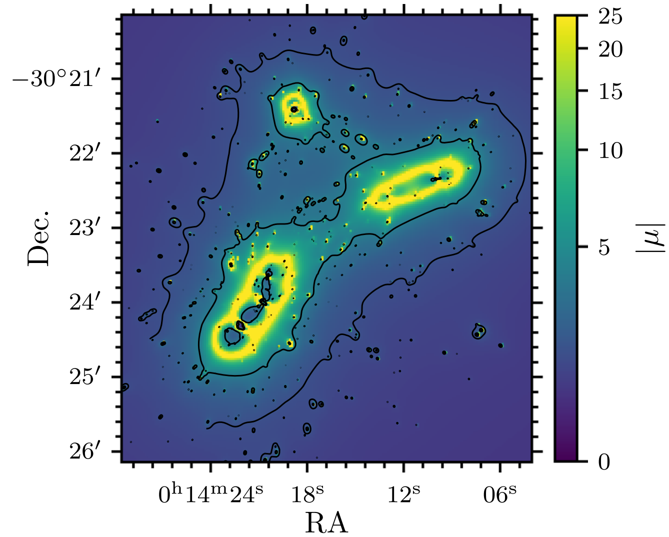

Figure 2. Total magnification map of our new `v2.0` SL model of A2744 for a source at redshift $z_s = 10$. The black contours represent magnification thresholds of $\mu = 2$ and $\mu = 4$.

3.3. Updating the UNCOVER Lens Model

We also use the UNCOVER spectroscopy to update the lens model of A2744 presented in L. J. Furtak et al. (2023b) and include the new `v2.0` model in the data release. As described in detail in Appendix B, this model incorporates the UNCOVER DR4 spectroscopic redshifts of multiple images, and all currently available JWST imaging for cluster member selection. In total, we added 14 spectroscopic redshifts compared to our initial `v1.0` model. The model is constructed with an updated version of the analytic lens modeling method by A. Zitrin et al. (2015). We refer the reader to Appendix B and L. J. Furtak et al. (2023b) for details of the parameterization for our lensing model of A2744.

With these constraints, the model achieves an average image reproduction error of $\Delta_{\rm rms} = 0\farcs60$, which is slightly better than our `v1.0` model ($\Delta_{\rm RMS} = 0\farcs66$; L. J. Furtak et al. 2023b). The critical lines and multiple image positions are shown in Figure 9 in Appendix B and we show an updated magnification map at source redshift $z_s = 10$ in Figure 2. We find the cluster to have a total critical area of $A_{\rm crit} = 0.63$ arcmin^2 for a source at $z_s = 2$. This translates to an effective Einstein radius of $\theta_E = 26\farcs9 \pm 2\farcs7$ enclosing a mass of $M(<\theta_E) = (1.0 \pm 0.2) \times 10^{14}\ M_\odot$. These also agree well with our measurements from our `v1.0` model

[40] An upscaling of $\times 1.3$ is used to account for the observed PRISM resolution improvement of compact sources compared to the STScI model, as found using `msafit` (A. de Graaff et al. 2024a).

[41] Public release of spectra and redshifts: https://jwst-uncover.github.io/DR4.html; also available from Zenodo (DR4.1.1): doi: 10.5281/zenodo.14559840.

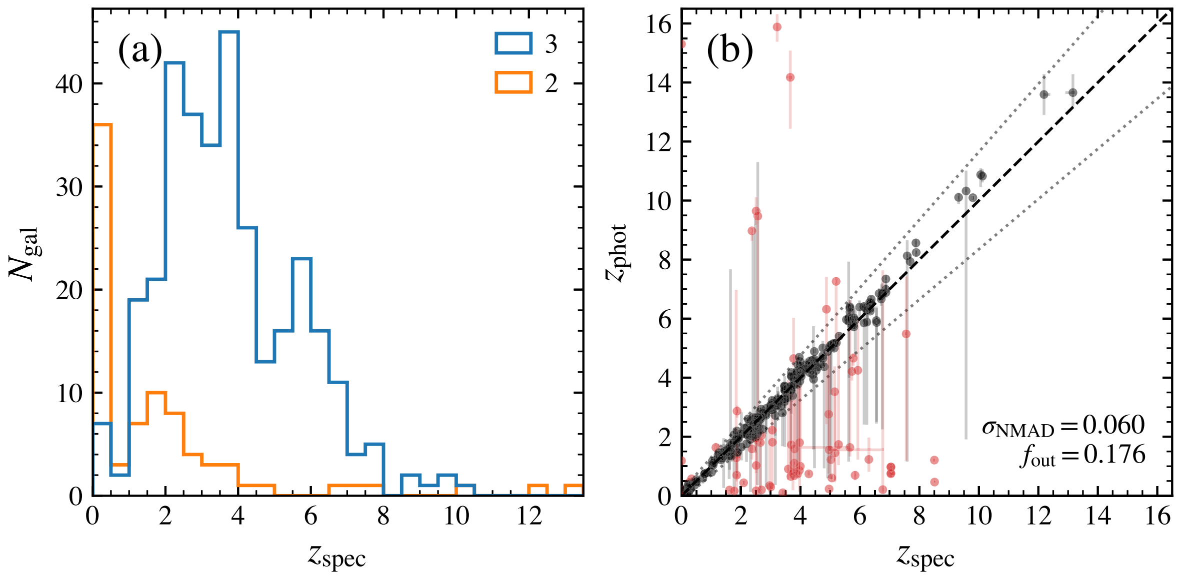

Figure 3. Redshift distribution of spectroscopically confirmed galaxies with robust redshifts (`flag_zspec_qual` $\geqslant 2$). (a): redshift histogram, split by redshift quality flag. (b): spectroscopic vs. photometric redshifts, using Prospector-β-derived $z_{\rm phot}$ from the internal v2.2.0 catalog (used during MSA target selection, including only HST and JWST/NIRCam broadband filters), with the uncertainties showing the 16th and 84th percentiles. Catastrophic outliers (with $|\Delta z| = (z_{\rm phot} - z_{\rm spec})/(1 + z_{\rm spec}) > 0.15$; boundary denoted with dotted lines) are colored red.

(L. J. Furtak et al. 2023b). Summing the surface mass density over the entire field (see Figure 9), we obtain a total cluster mass of $M_{\rm SL} = (2.1 \pm 0.3) \times 10^{15}\ M_{\odot}$. This is comparable to an M_{200} mass and thus places A2744 well within the mass range of typical clusters with the same Einstein radius (e.g., C. Fox et al. 2022).

The `v2.0` lens model is included in UNCOVER DR4. The public lensing products include deflection α, convergence κ, shear γ, magnification μ, and potential ψ maps, normalized to $D_{\rm ds}/D_{\rm s} = 1$, as well as catalogs of the cluster member galaxies and multiple images used. The JWST cluster member selection and spectroscopic redshifts of multiple images are further detailed in Appendices B.1 and B.2, respectively. We also updated the UNCOVER photometric and spectroscopic catalogs with magnification and shear parameters from the `v2.0` model. Individual models of each of the three substructures separately are also available on request, each achieving local image reproduction errors of $\Delta_{\rm RMS} \simeq 0\farcs2$.

4. Discussion

4.1. Success Rate and Redshift Distribution for Spectroscopically Confirmed Objects

The UNCOVER spectroscopic redshift catalog includes a 74% success rate, with robust redshifts (i.e., defined as `flag_zspec_qual` $\geqslant 2$; see Table 2 and Section 3.2) for 409 of the 553 targets with successfully observed and reduced spectra. A histogram of the redshift distribution of spectroscopically confirmed targets, split by `flag_zspec_qual`, is shown in Figure 3(a). We measure secure redshifts (based on two or more secure spectral features; `flag_zspec_qual` $= 3$) for 327 objects, spanning from $z \sim 0.3$ to $z \sim 10$. The 82 galaxies with solid redshifts (based on one broad continuum feature or two less robust features; `flag_zspec_qual` $= 2$) also span a wide redshift range ($z \sim 0.2-13$). This latter category includes most of the targeted galaxies in the A2744 cluster itself, as most have very red spectra with no emission lines and only a broad stellar bump (resulting in lower redshift precision).

We compare the spectroscopic and photometric redshifts for our sample of spectroscopically confirmed galaxies in Figure 3(b). We find the majority of the Prospector-β-derived $z_{\rm phot}$ (from the internal v2.2.0 catalog, the most up-to-date catalog used during MSA design in early summer 2023) are in good agreement with the measured $z_{\rm spec}$, with a low normalized median absolute deviation (NMAD) $\sigma_{\rm NMAD} = 0.060$. However, there is a relatively high fraction of catastrophic photometric redshift outliers (with $|\Delta z| = (z_{\rm phot} - z_{\rm spec})/(1 + z_{\rm spec}) > 0.15$; 17.6%, red circles).

Figure 4(a) shows that successfully observed spectroscopic targets with and without robust redshifts (`flag_zspec_qual` $\geqslant 2$ and <2, purple filled and gray open circles, respectively) have similar F277W – F444W colors. On average, targets without robust redshifts are fainter in F444W than spectroscopically confirmed objects, though both have overlapping distributions down to the very faintest magnitudes ($\mathrm{mag_{F444W}} \gtrsim 30$ AB). This is quantified in Figure 4(b), as the spectroscopic success fraction is very high for bright targets, but drops only to $\sim$30%–50% at $\mathrm{mag_{F444W}} \sim 29$ AB (excepting a few extremely faint targets at $\mathrm{mag_{F444W}} \gtrsim 30$ AB). The distributions of the targets with and without robustly measured redshifts suggest that while low S/N does contribute to failed spectroscopic confirmations, low S/N is not entirely responsible for the failed spectroscopic confirmations. Color likewise appears to not drive the failed $z_{\rm spec}$ measurements.

We similarly find catastrophic photometric redshift failures within of the spectroscopically confirmed sample ($|\Delta z| > 0.15$; shown with red points in Figure 3) are not primarily driven by low S/N or color, as these objects exhibit a wide range of magnitudes and F277W – F444W colors similar to the complete spectroscopically confirmed sample. Preliminary visual inspection suggests some of these outliers are due to confusion of the Lyman and Balmer breaks in the Prospector-β redshift fits; the outlier fraction is lower in the region with deep HST/ACS coverage, as rest-frame UV coverage at high redshifts helps to mitigate break confusion. Other outliers

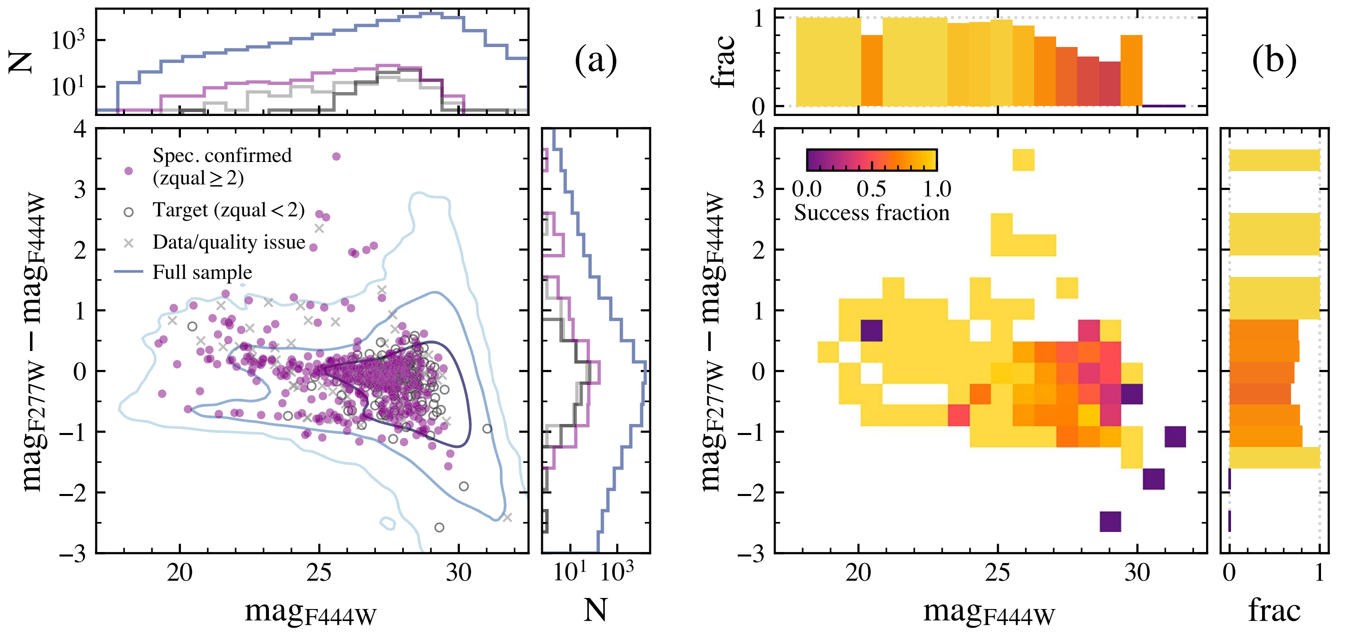

Figure 4. Distribution of the spectroscopic sample relative to the full UNCOVER photometric catalog (left) and the redshift measurement success rate (right) over total F444W magnitude vs. F277W – F444W color. All values are taken from the internal v2.2.0 catalog (used for designing masks). (a): points indicate the spectroscopically confirmed objects (`flag_zspec_qual` $\geqslant 2$; filled purple circles), targets without robust redshifts (`flag_zspec_qual` < 2; dark gray open circles), and targets with data quality issues (e.g., those on MSA1; gray crosses). Contours denote the parent photometric sample distribution (with `use_phot` $= 1$; see J. R. Weaver et al. 2024; 1σ, 2σ, and 3σ levels). Side panels show histograms over $\mathrm{mag_{F444W}}$ and F277W – F444W (line colors are the same as the points in the main panel). Though the sample selection incorporates multiple disparate categories, overall the targets follow the distribution of the parent sample down to $\mathrm{mag_{F444W}} \sim 29$ AB. Successfully observed targets without measured z_{spec} do not have systematically redder/bluer colors compared to the spectroscopically confirmed ones. The unconfirmed targets are fainter on average than the confirmed objects, though their distribution does overlap down to the very faintest magnitudes ($\mathrm{mag_{F444W}} \gtrsim 30$ AB). (b): 2D and 1D histograms of the redshift measurement success fraction over $\mathrm{mag_{F444W}}$ and F277W – F444W, defined as the fraction of objects with robust redshifts over the total number of successfully observed targets. The success fraction is very high over most of this space, though drops to ∼30%–50% at $\mathrm{mag_{F444W}} \sim 29$ AB.

may be explained by emission line boosting of the broadband photometry. We note that for the few very red targets (F277W – F444W $\gtrsim 1$), nearly all have catastrophic photometric redshift failures, suggesting additional spectral templates for photometric redshift fitting may be needed to capture the extreme colors of these objects.

A more detailed discussion of photometric redshift outliers relative to the measured z_{spec} will be presented in a forthcoming paper (see also K. A. Suess et al. 2024). This will include quantification of photometric redshift improvements by incorporating recently obtained medium-band imaging (from JWST-GO-4111; K. A. Suess et al. 2024)—which will better account for emission line boosting—and the inclusion of bluer coverage from NIRCam/F070W. Adding future deep UV HST/WFC3/UVIS F336W imaging from an approved program (HST-GO-17730; PIs: Whitaker, Bezanson, and Leja) will also help to improve photometric redshifts by mitigating break confusion.

4.2. Scientific Objectives Addressed by the UNCOVER Spectroscopic Sample

With a high redshift success rate (74% of targets with robust redshifts) and very deep spectra (up to 16.7 hr for five individual targets, and up to 38 hr with multiply lensed images of one object), these NIRSpec observations provide a treasure trove for studies ranging from galaxies within the A2744 cluster itself out to the first galaxies at Cosmic Dawn. We demonstrate the wide range of spectral features seen in the full UNCOVER sample of 409 galaxies with robust z_{spec}(`flag_zspec_qual` $\geqslant 2$) ranging from $z \sim 0.3$ to $z \sim 13$ in Figure 5. An incredible diversity of features can be seen in these ultradeep spectra: Paschen lines, He I 10833 Å, and the polycyclic aromatic hydrocarbon (PAH) 3.3 μm feature are seen in galaxies at the lowest redshifts, and [S III] 9068, 9531 Å are seen out to $z \sim 5$. Hα is detected out to $z \sim 7$, and Hβ and [O III] 4959, 5007 Å are seen in all galaxies except those at the very highest redshifts. The Balmer break is seen in galaxies at $z \gtrsim 1$, while the Lyman break (and Lyα) are seen at $z \gtrsim 4.5$.

An overview of the science cases addressed by the UNCOVER spectra is highlighted in Figure 6, showing a subset of objects from our sample. We have spectroscopically confirmed and begun characterizing the rest-frame UV spectra of 10 early galaxies at $z \geqslant 8.5$ (see, e.g., S. Fujimoto et al. 2023c), including two among the first generation of galaxies at $z_{\mathrm{spec}} = 13.03$ and $z_{\mathrm{spec}} = 12.39$ (as presented in B. Wang et al. 2023a). Our sample also features a number of early AGN at $z > 6$, including an X-ray-luminous AGN at $z_{\mathrm{spec}} = 10.1$ (A. D. Goulding et al. 2023; Á. Bogdán et al. 2024) and a broad-line AGN at $z_{\mathrm{spec}} = 8.5$ (V. Kokorev et al. 2023). Other targets include a number of dust-reddened, high-redshift objects described as "little red dots" (e.g., I. Labbe et al. 2023; L. J. Furtak et al. 2024a; J. E. Greene et al. 2024). The PRISM spectra also yield the first spectroscopic constraints on low-mass, low-luminosity galaxies during the Epoch of Reionization ($z \sim 6$–8), including direct constraints on the ionizing photon production efficiency that yield evidence that these faint galaxies are the primary drivers of the reionization of the Universe (H. Atek et al. 2024; P. Dayal et al. 2024), and extending the mass–metallicity relation to the low-mass end (I. Chemerynska et al. 2024a).

Our spectroscopic sample additionally includes a range of dusty galaxies out to $z \sim 4$, both with (e.g., some of the objects presented in V. Kokorev et al. 2023; S. H. Price et al. 2023) and without ALMA continuum detections (from, e.g., DUALZ;

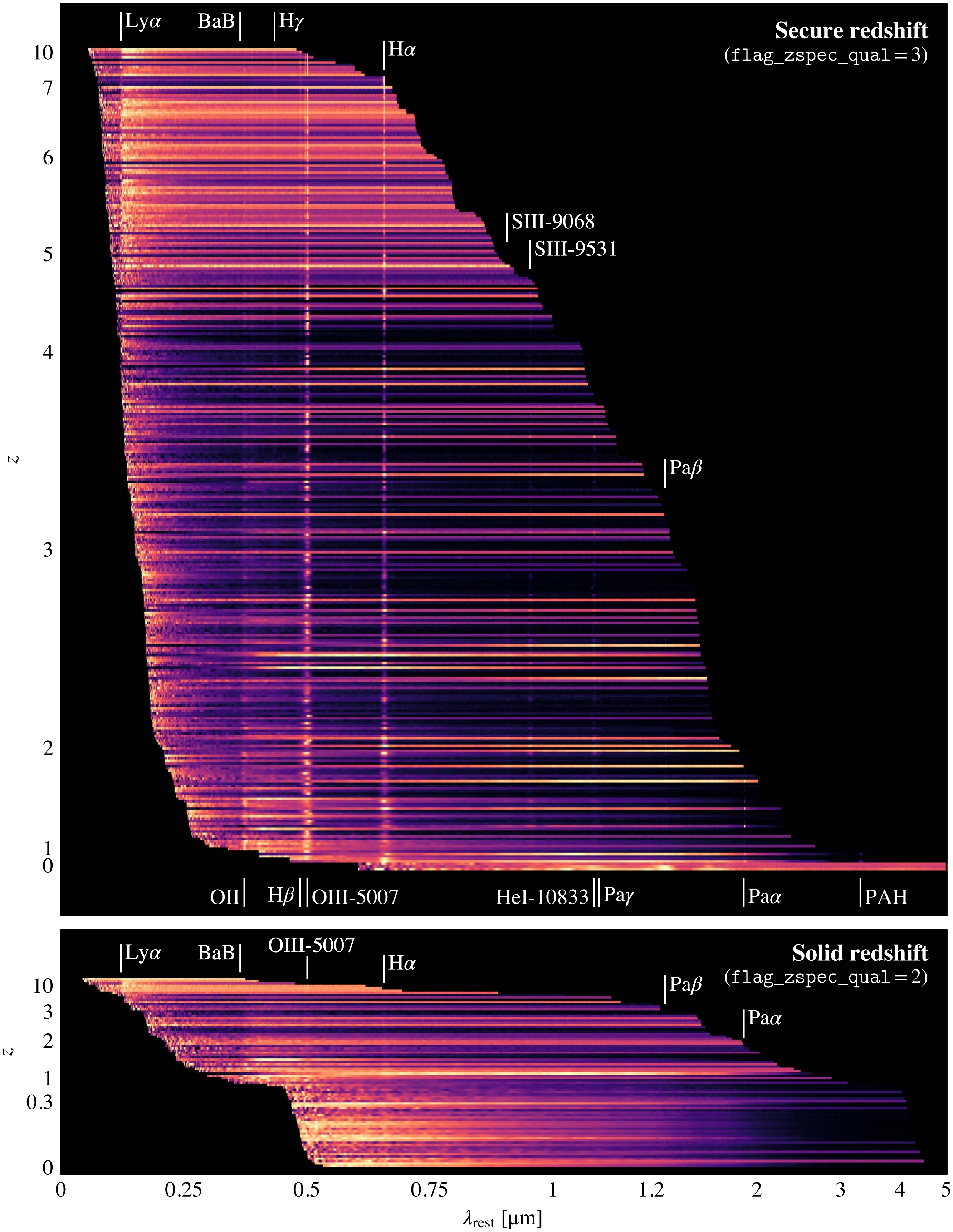

Figure 5. NIRSpec/PRISM spectra for all UNCOVER targets with secure (`flag_zspec_qual` = 3, $N = 327$; top) and solid (`flag_zspec_qual` = 2, $N = 82$; bottom) redshifts, shifted to the rest frame and ordered by increasing redshift. The wavelength axis is split, with linear and log scaling below and above 1.2 μm, respectively. The locations of notable emission and absorption/break features are annotated above and below the spectra.

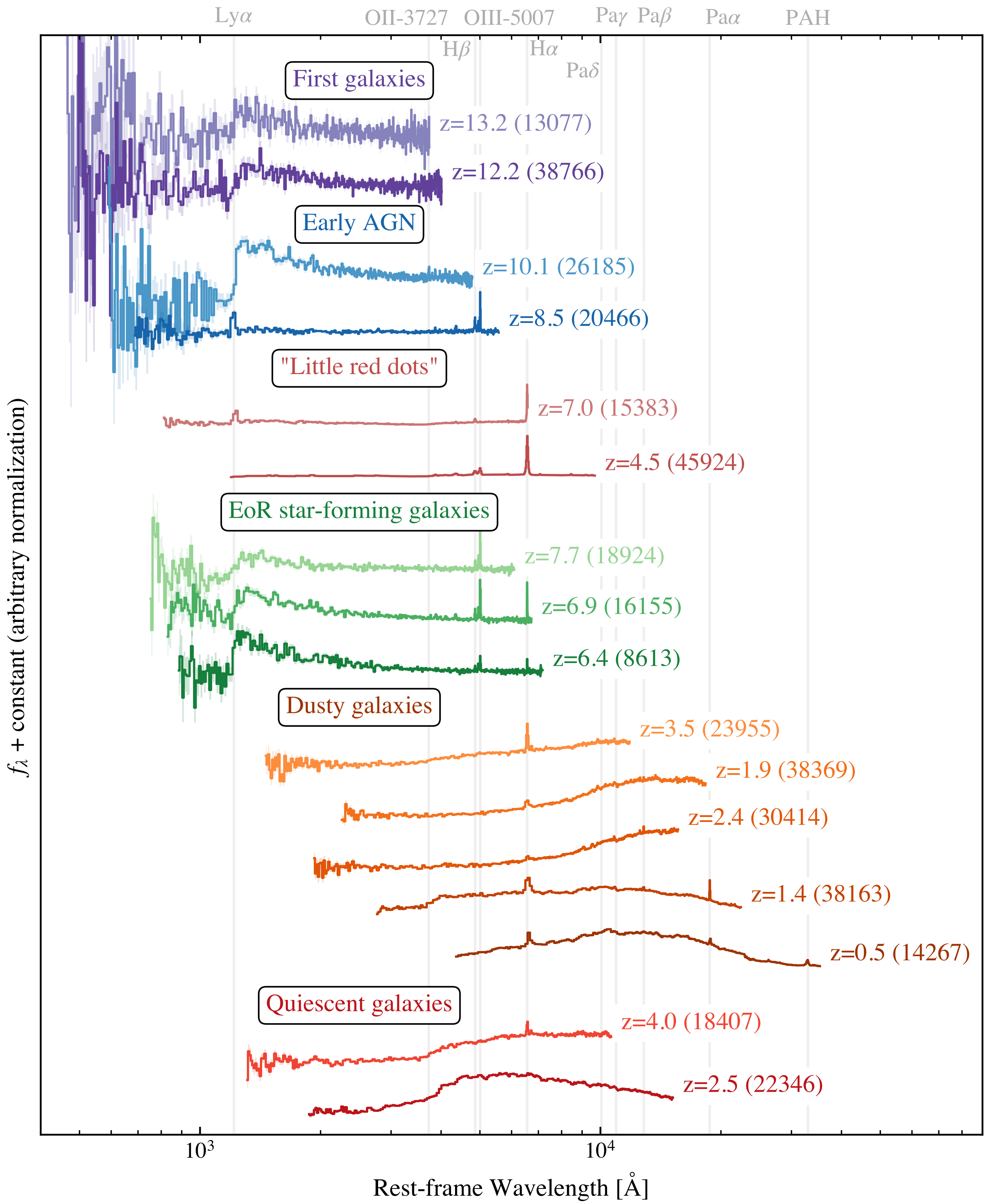

Figure 6. Overview of 1D spectra for a subset of our sample, highlighting key science themes addressed by the UNCOVER survey and mask design strategy. All spectra are shown in the rest frame in f_λ units (with arbitrary normalization and shifting), with the shaded contour denoting the uncertainty. The redshift and MSA ID of each object are annotated next to the spectra. Vertical lines mark the wavelengths of selected emission features.

S. Fujimoto et al. 2023). Two targeted galaxies at low redshift ($z \lesssim 0.5$) reveal detections of the 3.3 μm PAH emission feature and ice absorption features. Also targeted is a number of quiescent galaxies extending from low redshift to $z \gtrsim 3$. This includes a massive, dusty quiescent galaxy confirmed at $z_{\rm spec} = 3.97$ (D. J. Setton et al. 2024), with the deep PRISM spectra revealing its detailed star formation history, which indicates the early formation of its dense stellar core. Finally, we obtained spectra for three brown dwarfs located within our own Milky Way (D. Langeroodi & J. Hjorth 2023; A. J. Burgasser et al. 2024): one explicitly targeted, and two that were selected based on the photometric criteria for dust-reddened "little red dots" and AGN at high redshift. These deep spectra reveal the spectral classifications, temperatures, and metallicities, as well as characterizing molecular features within the brown dwarf atmospheres.

5. Final Remarks

The ultradeep PRISM spectra from the UNCOVER program add immense value to the already rich—and still growing—treasure trove of public observations of the A2744 lensing cluster field. This first data release of the 1D and 2D spectra (with local background subtraction), along with derived catalogs with quality flags, is publicly available on the survey website at https://jwst-uncover.github.io/DR4.html. Future spectroscopic releases will include the repeat observations of MSA1 and spectra accompanying the Visit 3 repeat of the NIRCam parallel imaging (observed 2024 July 30–31). Additional improvements in the reduction and released products will include global background subtraction and more sophisticated modeling of emission lines.

Acknowledgments

We thank the referee for a constructive and insightful report, which has improved this manuscript. This work is based in part on observations made with the NASA/ESA/CSA James Webb Space Telescope. The data were obtained from the Mikulski Archive for Space Telescopes at the Space Telescope Science Institute, which is operated by the Association of Universities for Research in Astronomy, Inc., under NASA contract NAS 5-03127 for JWST. These observations are associated with JWST-GO-2561. Support for program JWST-GO-2561 was provided by NASA through a grant from the Space Telescope Science Institute, which is operated by the Associations of Universities for Research in Astronomy, Incorporated, under NASA contract NAS 5-26555. The specific observations analyzed can be accessed via doi:10.17909/8k5c-xr27. Cloud-based data processing and file storage for this work are provided by the AWS Cloud Credits for Research program. This research was supported in part by the University of Pittsburgh Center for Research Computing, RRID:SCR_022735, through the resources provided. Specifically, this work used the H2P cluster, which is supported by NSF award number OAC-2117681. The Cosmic Dawn Center is funded by the Danish National Research Foundation (DNRF) under grant #140. The BGU lensing group acknowledges support by grant No. 2020750 from the United States-Israel Binational Science Foundation (BSF) and grant No. 2109066 from the United States National Science Foundation (NSF), by the Israel Science Foundation grant No. 864/23, and by the Ministry of Science & Technology, Israel.

Facility: JWST (NIRSpec, NIRCam).

Software: astropy (Astropy Collaboration et al. 2013, 2018; Astropy Collaboration et al. 2022), eMPT (N. Bonaventura et al. 2023), `jwst` pipeline (v1.14.0; H. Bushouse et al. 2024), `msaexp` (v0.8.5; G. Brammer 2023a), `grizli` (v1.11.9; G. Brammer 2023b), EAZY (G. B. Brammer et al. 2008), matplotlib (J. D. Hunter 2007), numpy (C. R. Harris et al. 2020), scipy (P. Virtanen et al. 2020), seaborn (M. Waskom et al. 2017), `snowblind` (J. Davies 2024).

Appendix A
Parallel NIRCam Imaging

Coordinated parallel NIRCam imaging was taken simultaneously with the primary NIRSpec/PRISM multiobject spectroscopy. Altogether imaging was taken in seven broadband and two medium-band filters (see Table 3), using the MEDIUM8 readout pattern for all exposures. This parallel imaging overlaps existing HST/ACS and WFC3 observations

Table 3
NIRCam Parallel Imaging

Filter (1)	Exposure (hr) (2)	Total Area (arcmin^2) (3)	5σ Depth (AB) (4)	Masks (5)
F090W	2.8	9.2	28.94	5
F115W	0.9–5.9	26.8	28.54	1–6
F150W	0.9–5.0	25.9	28.71	1–2, 4, 6, 7[a]
F200W	0.9–5.0	25.9	28.91	1–2, 4, 6, 7[a]
F277W	0.9–5.9	26.9	28.96	1–6
F356W	0.9–5.0	26.2	29.02	1–2, 4, 6, 7[a]
F410M	1.4	9.3	28.85	5
F444W	0.9–5.0	26.2	28.62	1–2, 4, 6, 7[a]
F480M	1.4	9.3	28.07	5

Notes. Depths are calculated within 0.″16 and 0.″32 diameter apertures in the short-wavelength and LW bands, respectively, using noise properties derived from the weight maps and corrected to total assuming a point-source geometry. As the footprint is inhomogeneous, these estimates correspond to a 0.7 arcmin^2 box centered at (3.6012969, −30.4908199). Column (1): NIRCam filter. Column (2): filter exposure time across footprint (hr). Column (3): total filter footprint area (arcmin^2). Column (4): imaging 5σ depth. Column (5): mask(s) with which the filter was observed in parallel.

[a] Parallel imaging in F150W, F200W, F356W, and F444W in Visit 3 (Mask 3) was lost due to an SSR drive exception (see Section 2.2). Repeat observations were taken on 2024 July 31.

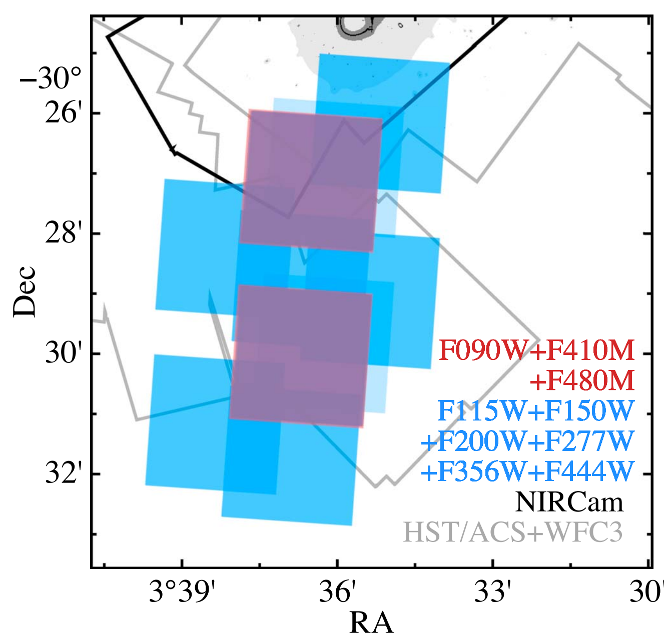

Figure 7. The NIRCam parallel footprints, plotted over the existing NIRCam and HST/ACS + WFC3 coverage footprints and the lensing contours as shown in Figure 1. Coverage of F090W, F410M, and F480M is restricted to Visit 5 (taken in parallel to Mask 5) and is shown in red, and all other filters with full parallel pointing coverage (F115W, F150W, F200W, F277W, F356W, and F444W) are shown in blue.

(HFF, J. M. Lotz et al. 2017; BUFFALO, C. L. Steinhardt et al. 2020; see Figure 7). The cumulative exposure time per filter over the parallel footprint ranges from 0.9 to 5.9 hr, with total areas ranging from 9.2 to 26.9 arcmin^2. This includes imaging in six of the broadband filters that cover the full parallel area (excepting observation issues), and imaging in F090W and the two medium-band F410M and F480M that were only taken in parallel with Mask 5 (see Table 3).

Appendix B
Updates to the UNCOVER Strong Lensing Model of A2744

We use the UNCOVER spectroscopy, described in this work, as well new JWST/NIRCam imaging (K. A. Suess et al. 2024) and grism spectroscopy (R. P. Naidu et al. 2024) of the A2744 field to update the UNCOVER SL model of the cluster, as presented in Section 3.3.

The parametric lens model of A2744 is constructed with an updated version of the A. Zitrin et al. (2015) analytical method. It comprises five smooth cluster-scale dark matter halos centered on each of the subclusters' brightest cluster galaxy, modeled as pseudoisothermal elliptical mass distributions (A. Kassiola & I. Kovner 1993), and 552 cluster member galaxies (see Appendix B.1), modeled as dual pseudoisothermal ellipsoids (Á. Elìasdóttir et al. 2007). We refer the reader to L. J. Furtak et al. (2023b) for more details on the implementation and setup of our A2744 model.

While the currently available `v1.1` SL model presented in L. J. Furtak et al. (2023b) is based on HST-selected cluster members and mostly photometric multiple image systems in the northern and northwestern extended cluster substructures, the `v2.0` model presented here adds additional cluster member galaxies selected with JWST (Appendix B.1) and new spectroscopic redshifts of multiple image systems as constraints (Appendix B.2). The new SL model (Section 3.3) maps are also made public on the UNCOVER website in the framework of DR4[42] (see Section 3.3).

B.1. JWST Cluster Member Selection

Thanks to the JWST Medium Bands, Mega Science (MegaScience) program (K. A. Suess et al. 2024), we now have NIRCam F070W and F090W imaging data covering the entire UNCOVER field at our disposal. These two filters straddle the 4000 Å break at the cluster's redshift $z_d = 0.308$ and are therefore ideally suited for photometric selection of cluster members from the red sequence (e.g., A. Repp & H. Ebeling 2018). We use `SExtractor` (E. Bertin & S. Arnouts 1996) in dual-imaging mode to detect sources in the F090W mosaic and measure their photometry in F070W and F090W. Following our approach in L. J. Furtak et al. (2023b, 2024b), we then use the colors of the known spectroscopic cluster members from P. Bergamini et al. (2023b) to calibrate the cluster's red sequence in the color–magnitude diagram (see Figure 8). Cluster members are then selected in a color window of width 0.1 around the red sequence and brighter than 23 mag in the F090W band. The resulting sample is crossmatched with the known spectroscopic and HST-selected cluster members (L. J. Furtak et al. 2023b) to make sure no galaxy is doubly counted.

42 https://jwst-uncover.github.io/DR4.html

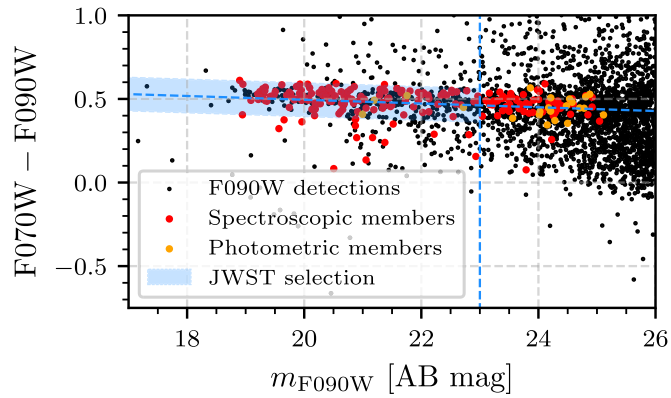

Figure 8. JWST/NIRCam color–magnitude diagram of objects detected in A2744, showing the cluster's red sequence. Known spectroscopic and photometric cluster members from P. Bergamini et al. (2023b) are shown as red and orange dots, and our red sequence selection is shown as the blue shaded area.

Table 4
New Spectroscopic Redshifts of Multiply Imaged Sources Included in Our `v2.0` SL Model of A2744

System ID (1)	MSA ID (2)	$z_{\rm spec}$ (3)	Redshift Reference (4)
UNCOVER Spectroscopy			
53	13123	7.045	L. J. Furtak et al. (2024a)
65	60046	3.519	This work
67	33295	2.322	J. C. Siegel et al. (2025, in preparation)
69	29315	2.411	This work
70	60053	2.392	This work
72	60061	3.747	This work
74	60067	2.374	This work
78	60018	2.315	This work
80	60010	3.672	C. C. Williams et al. (2025, in preparation)
81	60081	3.479	This work
86	16155	6.875	H. Atek et al. (2024)
ALT Spectroscopy			
84	11254	6.873	R. P. Naidu et al. (2024)
85	⋯	4.753	R. P. Naidu et al. (2024)
VLT/MUSE Spectroscopy			
68	⋯	2.584	P. Bergamini et al. (2023a)

Note. A full table of multiple images used in the `v2.0` model is included in the public SL model release at https://jwst-uncover.github.io/DR4.html. Column (1): ID number of the multiple image system. Column (2): ID number of the MSA slit on one of the images. Column (3): spectroscopic redshift. Column (4): reference to the spectroscopic redshift measurement.

As a result, we complement our previous cluster member sample from L. J. Furtak et al. (2023b) with 132 new NIRCam-selected cluster members. This bring the total number of cluster members included in the SL model to 552, now spanning the entire 45 arcmin^2 of the UNCOVER field. The new, NIRCam-selected sample in particular adds cluster members in the northeast to northwest of the cluster, areas which were not covered with HST.

B.2. New Spectroscopic Redshifts of Multiple Images

The unprecedented depth and areal coverage of the UNCOVER survey's imaging (R. Bezanson et al. 2024)

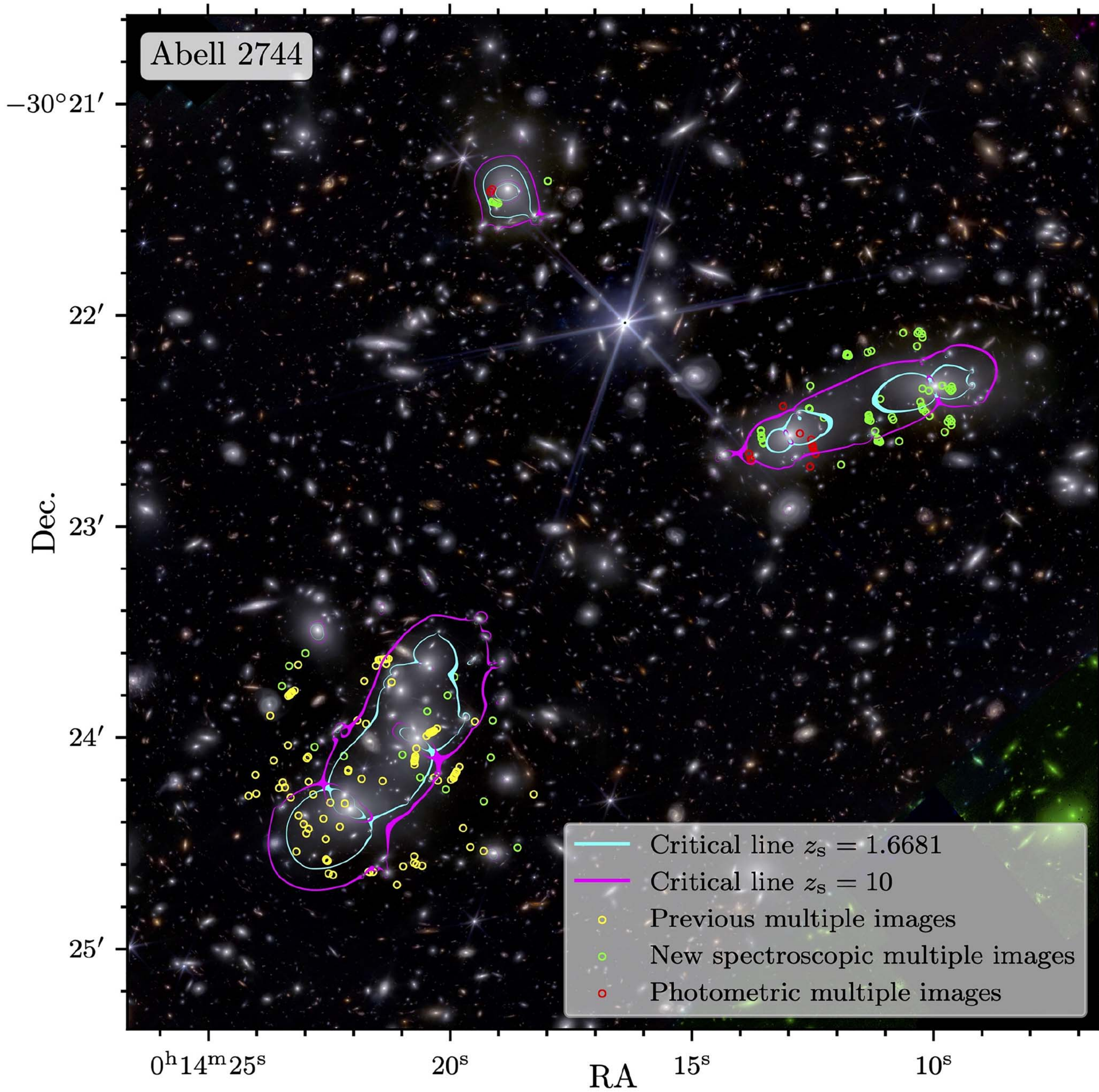

Figure 9. A 4.′3 × 4.′8 cutout of an UNCOVER and MegaScience NIRCam composite-color image of A2744 including all broad and medium bands. Overlaid we show the critical curves of our SL model for source redshifts $z_s = 1.6881$ (corresponding to system 1) and $z_s = 10$ in blue and purple, respectively. Multiple images from P. Bergamini et al. (2023b), used with spectroscopic redshifts in our `v1.0` model, are shown in yellow, and multiple images with new spectroscopic redshifts in our `v2.0` model are shown in green. Photometric multiple images are shown in red. The area between the main cluster and the northwestern substructure in particular has high magnifications of order $\mu \gtrsim 4$ for sources at $z_s = 10$ (see Figure 2). Note, a vectorized full 0.″04 pixel^{-1} resolution version of this figure is included in the public `v2.0` SL model release.

enabled us to detect new multiple image systems in northwestern and northern extensions of A2744, which were previously not know to be dense enough to produce SL (L. J. Furtak et al. 2023b). These new systems were however not constrained with spectroscopic redshifts in the first UNCOVER model (`v1.0`) due to the lack of spectroscopic coverage in those areas. Multiple images without precise redshift information are known to significantly bias SL models of galaxy clusters (e.g., T. L. Johnson & K. Sharon 2016), which is why spectroscopic redshifts are paramount for accurate SL modeling and magnification estimates.

After the publication of our `v1.0` model (L. J. Furtak et al. 2023b), new VLT/MUSE observations found system 68 to lie at $z_{\rm spec} = 2.584$ (P. Bergamini et al. 2023a). We included that new redshift in our `v1.1` model release in 2023 June, but the model remained mostly constrained with photometric systems in the northwest and the north. With the UNCOVER JWST/NIRSpec observations presented in this work, we are now able to spectroscopically confirm numerous multiple image systems in the whole UNCOVER field. In total, we obtained 10 new spectroscopic redshifts. These in particular include the triply imaged high-redshift AGN A2744-QSO1 at $z_{\rm spec} = 7.045$

(system 53; L. J. Furtak et al. 2024a), a low-mass heavily star-forming object at $z_{spec} = 6.875$ (system 86; H. Atek et al. 2024), and a massive quiescent galaxy at $z_{spec} = 2.322$ stretched into an arc (system 67; J. C. Siegel et al. 2025, in preparation). In addition, the JWST Cycle 2 program All the Little Things (ALT; Program ID 3516, PIs: Matthee and Naidu) observed the A2744 field with JWST/NIRCam grism spectroscopy in the F356W filter, which enabled the discovery of two new multiple image systems at $z_{spec} = 6.873$ (system 84) and $z_{spec} = 4.753$ (system 85), respectively (R. P. Naidu et al. 2024), which we also included in the model. Note that system 84 also has an UNCOVER NIRSpec redshift which agrees with the ALT redshifts.

We list all new multiple image redshifts in Table 4 and show them in Figure 9. In total, our new `v2.0` SL model is constrained by 187 multiple images belonging to 66 individual sources. Of these, 60 sources now have spectroscopic redshifts, leaving only six multiply imaged sources with free redshifts in the model. For additional constraining power, we now also use parity information of four very close knot systems, systems 65.3, 67.3, 78.3, and 80.2, as constraints in the model (see Equations (8) and (9) in L. J. Furtak et al. 2023b). A full list of multiple images, including coordinates and redshifts, is included in the public `v2.0` SL model release.

ORCID iDs

Sedona H. Price https://orcid.org/0000-0002-0108-4176
Rachel Bezanson https://orcid.org/0000-0001-5063-8254
Ivo Labbe https://orcid.org/0000-0002-2057-5376
Lukas J. Furtak https://orcid.org/0000-0001-6278-032X
Anna de Graaff https://orcid.org/0000-0002-2380-9801
Jenny E. Greene https://orcid.org/0000-0002-5612-3427
Vasily Kokorev https://orcid.org/0000-0002-5588-9156
David J. Setton https://orcid.org/0000-0003-4075-7393
Katherine A. Suess https://orcid.org/0000-0002-1714-1905
Gabriel Brammer https://orcid.org/0000-0003-2680-005X
Sam E. Cutler https://orcid.org/0000-0002-7031-2865
Joel Leja https://orcid.org/0000-0001-6755-1315
Richard Pan https://orcid.org/0000-0002-9651-5716
Bingjie Wang (王冰洁) https://orcid.org/0000-0001-9269-5046
John R. Weaver https://orcid.org/0000-0003-1614-196X
Katherine E. Whitaker https://orcid.org/0000-0001-7160-3632
Hakim Atek https://orcid.org/0000-0002-7570-0824
Adam J. Burgasser https://orcid.org/0000-0002-6523-9536
Iryna Chemerynska https://orcid.org/0009-0009-9795-6167
Pratika Dayal https://orcid.org/0000-0001-8460-1564
Robert Feldmann https://orcid.org/0000-0002-1109-1919
Natascha M. Förster Schreiber https://orcid.org/0000-0003-4264-3381
Yoshinobu Fudamoto https://orcid.org/0000-0001-7440-8832
Seiji Fujimoto https://orcid.org/0000-0001-7201-5066
Karl Glazebrook https://orcid.org/0000-0002-3254-9044
Andy D. Goulding https://orcid.org/0000-0003-4700-663X
Gourav Khullar https://orcid.org/0000-0002-3475-7648
Mariska Kriek https://orcid.org/0000-0002-7613-9872
Danilo Marchesini https://orcid.org/0000-0001-9002-3502
Michael V. Maseda https://orcid.org/0000-0003-0695-4414
Tim B. Miller https://orcid.org/0000-0001-8367-6265
Adam Muzzin https://orcid.org/0000-0002-9330-9108
Themiya Nanayakkara https://orcid.org/0000-0003-2804-0648
Erica Nelson https://orcid.org/0000-0002-7524-374X
Pascal A. Oesch https://orcid.org/0000-0001-5851-6649
Heath Shipley https://orcid.org/0009-0007-1787-2306
Renske Smit https://orcid.org/0000-0001-8034-7802
Edward N. Taylor https://orcid.org/0000-0002-5522-9107
Pieter van Dokkum https://orcid.org/0000-0002-8282-9888
Christina C. Williams https://orcid.org/0000-0003-2919-7495
Adi Zitrin https://orcid.org/0000-0002-0350-4488

References

Adams, N. J., Conselice, C. J., Austin, D., et al. 2024, ApJ, 965, 169
Arrabal Haro, P., Dickinson, M., Finkelstein, S. L., et al. 2023a, ApJL, 951, L22
Arrabal Haro, P., Dickinson, M., Finkelstein, S. L., et al. 2023b, Natur, 622, 707
Astropy Collaboration, Price-Whelan, A. M., Lim, P. L., et al. 2022, ApJ, 935, 167
Astropy Collaboration, Price-Whelan, A. M., Sipőcz, B. M., et al. 2018, AJ, 156, 123
Astropy Collaboration, Robitaille, T. P., Tollerud, E. J., et al. 2013, A&A, 558, A33
Atek, H., Chemerynska, I., Wang, B., et al. 2023, MNRAS, 524, 5486
Atek, H., Labbé, I., Furtak, L. J., et al. 2024, Natur, 626, 975
Austin, D., Adams, N., Conselice, C. J., et al. 2023, ApJL, 952, L7
Barro, G., Pérez-González, P. G., Kocevski, D. D., et al. 2024, ApJ, 963, 128
Bergamini, P., Acebron, A., Grillo, C., et al. 2023a, ApJ, 952, 84
Bergamini, P., Acebron, A., Grillo, C., et al. 2023b, A&A, 670, A60
Bertin, E., & Arnouts, S. 1996, A&AS, 117, 393
Bezanson, R., Labbe, I., Whitaker, K. E., et al. 2024, ApJ, 974, 92
Bogdán, Á., Goulding, A. D., Natarajan, P., et al. 2024, NatAs, 8, 126
Böker, T., Beck, T. L., Birkmann, S. M., et al. 2023, PASP, 135, 038001
Bonaventura, N., Jakobsen, P., Ferruit, P., Arribas, S., & Giardino, G. 2023, A&A, 672, A40
Bradley, L. D., Coe, D., Brammer, G., et al. 2023, ApJ, 955, 13
Brammer, G. 2023a, msaexp: NIRSpec Analyis Tools, v0.6.17, Zenodo, doi:10.5281/zenodo.7299500
Brammer, G. 2023b, grizli, v1.9.11, Zenodo, doi:10.5281/zenodo.1146904
Brammer, G. B., van Dokkum, P. G., & Coppi, P. 2008, ApJ, 686, 1503
Burgasser, A. J., Bezanson, R., Labbe, I., et al. 2024, ApJ, 962, 177
Bushouse, H., Eisenhamer, J., Dencheva, N., et al. 2024, JWST Calibration Pipeline, v1.14.0, Zenodo, doi:10.5281/zenodo.10870758
Carnall, A. C., Cullen, F., McLure, R. J., et al. 2024, MNRAS, 534, 325
Carnall, A. C., McLeod, D. J., McLure, R. J., et al. 2023a, MNRAS, 520, 3974
Carnall, A. C., McLure, R. J., Dunlop, J. S., et al. 2023b, Natur, 619, 716
Casey, C. M., Akins, H. B., Shuntov, M., et al. 2024, ApJ, 965, 98
Chemerynska, I., Atek, H., Dayal, P., et al. 2024a, ApJL, 976, L15
Chemerynska, I., Atek, H., Furtak, L. J., et al. 2024b, MNRAS, 531, 2615
Claeyssens, A., Adamo, A., Richard, J., et al. 2023, MNRAS, 520, 2180
Curtis-Lake, E., Carniani, S., Cameron, A., et al. 2023, NatAs, 7, 622
Davies, J., 2024 snowblind, v0.2.1, Github, https://github.com/mpi-astronomy/snowblind
Dayal, P., Volonteri, M., Greene, J. E., et al. 2024, arXiv:2401.11242
de Graaff, A., Rix, H.-W., Carniani, S., et al. 2024a, A&A, 684, A87
de Graaff, A., Setton, D. J., Brammer, G., et al. 2024b, NatAs, 9, 280
Elìasdóttir, Á., Limousin, M., Richard, J., et al. 2007, arXiv:0710.5636
Ferreira, L., Adams, N., Conselice, C. J., et al. 2022, ApJL, 938, L2
Ferreira, L., Conselice, C. J., Sazonova, E., et al. 2023, ApJ, 955, 94
Ferruit, P., Jakobsen, P., Giardino, G., et al. 2022, A&A, 661, A81
Finkelstein, S. L., Bagley, M. B., Ferguson, H. C., et al. 2023, ApJL, 946, L13
Forbes, D. A., & Romanowsky, A. J. 2023, MNRAS, 520, L58
Fox, C., Mahler, G., Sharon, K., & Remolina González, J. D. 2022, ApJ, 928, 87
Fruchter, A. S., & Hook, R. N. 2002, PASP, 114, 144
Fujimoto, S., Bezanson, R., Labbe, I., et al. 2023, arXiv:2309.07834
Fujimoto, S., Kohno, K., Ouchi, M., et al. 2024a, ApJS, 275, 36
Fujimoto, S., Wang, B., Weaver, J., et al. 2024b, ApJ, 977, 250
Furtak, L. J., Labbé, I., Zitrin, A., et al. 2024a, Natur, 628, 57
Furtak, L. J., Zitrin, A., Plat, A., et al. 2023a, ApJ, 952, 142
Furtak, L. J., Zitrin, A., Richard, J., et al. 2024b, MNRAS, 533, 2242
Furtak, L. J., Zitrin, A., Weaver, J. R., et al. 2023b, MNRAS, 523, 4568

Glazebrook, K., Nanayakkara, T., Schreiber, C., et al. 2024, Natur, 628, 277
Goulding, A. D., Greene, J. E., Setton, D. J., et al. 2023, ApJL, 955, L24
Greene, J. E., Labbe, I., Goulding, A. D., et al. 2024, ApJ, 964, 39
Harikane, Y., Zhang, Y., Nakajima, K., et al. 2023, ApJ, 959, 39
Harris, C. R., Millman, K. J., van der Walt, S. J., et al. 2020, Natur, 585, 357
Harris, W. E., & Reina-Campos, M. 2023, MNRAS, 526, 2696
Harris, W. E., & Reina-Campos, M. 2024, ApJ, 971, 155
Horne, K. 1986, PASP, 98, 609
Hunter, J. D. 2007, CSE, 9, 90
Johnson, T. L., & Sharon, K. 2016, ApJ, 832, 82
Kartaltepe, J. S., Rose, C., Vanderhoof, B. N., et al. 2023, ApJL, 946, L15
Kassiola, A., & Kovner, I. 1993, ApJ, 417, 450
Kokorev, V., Caputi, K. I., Greene, J. E., et al. 2024, ApJ, 968, 38
Kokorev, V., Fujimoto, S., Labbe, I., et al. 2023, ApJL, 957, L7
Labbe, I., Greene, J. E., Bezanson, R., et al. 2025, ApJ, 978, 978
Langeroodi, D., & Hjorth, J. 2023, ApJL, 957, L27
Lotz, J. M., Koekemoer, A., Coe, D., et al. 2017, ApJ, 837, 97
Maiolino, R., Scholtz, J., Curtis-Lake, E., et al. 2024, A&A, 691, A145
Martorano, M., van der Wel, A., Bell, E. F., et al. 2023, ApJ, 957, 46
Matthee, J., Naidu, R. P., Brammer, G., et al. 2024, ApJ, 963, 129
Mowla, L., Iyer, K. G., Desprez, G., et al. 2022, ApJL, 937, L35
Muñoz Arancibia, A. M., González-López, J., Ibar, E., et al. 2023, A&A, 675, A85
Naidu, R. P., Oesch, P. A., van Dokkum, P., et al. 2022, ApJL, 940, L14
Naidu, R. P., Matthee, J., Kramarenko, I., et al. 2024, arXiv:2410.01874
Nelson, E. J., Suess, K. A., Bezanson, R., et al. 2023, ApJL, 948, L18
Oke, J. B. 1974, ApJS, 27, 21
Pérez-González, P. G., Costantin, L., Langeroodi, D., et al. 2023, ApJL, 951, L1
Price, S. H., Suess, K. A., Williams, C. C., et al. 2025, ApJ, 980, 11
Repp, A., & Ebeling, H. 2018, MNRAS, 479, 844
Rieke, M. J., Kelly, D. M., Misselt, K., et al. 2023, PASP, 135, 028001
Roberts-Borsani, G., Treu, T., Chen, W., et al. 2023, Natur, 618, 480
Robertson, B., Johnson, B. D., Tacchella, S., et al. 2024, ApJ, 970, 31
Robertson, B. E., Tacchella, S., Johnson, B. D., et al. 2023, NatAs, 7, 611
Setton, D. J., Khullar, G., Miller, T. B., et al. 2024, ApJ, 974, 145
Steinhardt, C. L., Jauzac, M., Acebron, A., et al. 2020, ApJS, 247, 64
Suess, K. A., Williams, C. C., Robertson, B., et al. 2023, ApJL, 956, L42
Suess, K. A., Weaver, J. R., Price, S. H., et al. 2024, ApJ, 976, 101
Treu, T., Roberts-Borsani, G., Bradac, M., et al. 2022, ApJ, 935, 110
Valentino, F., Brammer, G., Gould, K. M. L., et al. 2023, ApJ, 947, 20
van der Wel, A., Martorano, M., Häußler, B., et al. 2024, ApJ, 960, 53
Virtanen, P., Gommers, R., Oliphant, T. E., et al. 2020, NatMe, 17, 261
Wang, B., Fujimoto, S., Labbé, I., et al. 2023a, ApJL, 957, L34
Wang, B., Leja, J., Bezanson, R., et al. 2023b, ApJL, 944, L58
Wang, B., Leja, J., Labbé, I., et al. 2024, ApJS, 270, 12
Waskom, M., Botvinnik, O., O'Kane, D., et al. 2017, Mwaskom/Seaborn: v0.8.1, Zenodo, doi:10.5281/zenodo.883859
Weaver, J. R., Cutler, S. E., Pan, R., et al. 2024, ApJS, 270, 7
Williams, C. C., Alberts, S., Ji, Z., et al. 2024, ApJ, 968, 34
Wu, Y., Cai, Z., Sun, F., et al. 2023, ApJL, 942, L1
Zitrin, A., Fabris, A., Merten, J., et al. 2015, ApJ, 801, 44